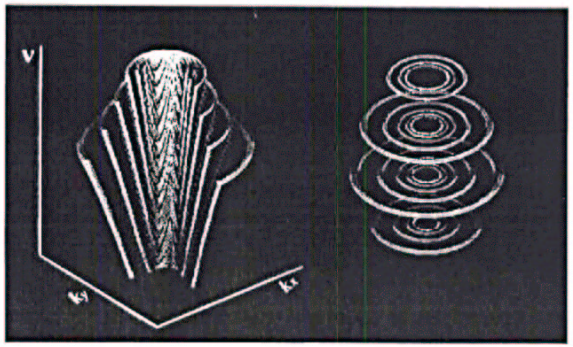

Figure 1. Model of a 3-dimensional power spectrum of medium-high ℓ solar acoustic modes. Each surface corresponds to a specific ν value. On the right the rings of power in a frequency cut are shown.

3. REDUCTION PROCESS

To track the sections over time, we used the model for the photospheric differential rotation:

$$\Omega = a_0 - a_2 \cdot \cos^2(\phi) - a_4 \cdot \cos^4(\phi) - s_0 \,, \quad (1)$$

where ϕ is the colatitude and $a_0 = 452.0$ nHz, $a_2 = 49.0$ nHz, $a_4 = 84.0$ nHz the coefficients given by Snodgrass (1984). $s_0 = 31.7$ nHz is the sidereal to synodic correction. We assumed that the rotation rate of each section corresponds to that of its center. After tracking, the section is mapped into an azimuthal equidistant projection, which has shown to be the most appropriate coordinate system for the plane-wave approximation (Haber, 1995).

Once the sections have been tracked and remapped, the sequences of images are Fourier transformed in both the x and y spatial directions and in time to obtain the 3-dimensional power spectra. The spectra have a spatial frequency resolution of 3.37×10^{-2} Mm^{-1} and a temporal frequency resolution of 10.85 μHz.

4. FITTING METHOD AND INVERSION PROCESS

4.1. Fitting Method

The method used to fit the 3-dimensional spectra is based on the model of Anderson et al. (1990) for a Lorentzial profile of the solar oscillation spectra peaks. It was adapted by Patrón (1994). In this model, the spectral power is given by:

$$P_n(\nu, k_x, k_y) = \frac{A^2}{\left[\nu - \left(\nu_{nl} + \frac{c_1 k_x + c_2 k_y}{2\pi}\right)\right]^2 + \sigma^2} + b_1 k^{-3} + b_2 k^{-4} \,,$$

where A and σ describe the amplitude and half-width at half-maximum of the Lorentzian, b_1 and b_2 parameterize the background, and c is the constant of the dispersion relation ($\omega = c\left(k_x^2 + k_y^2\right)^{\frac{1}{2}}$). n is the radial order considered; we fit 2 orders simultaneously, so the expression becomes a summation of the contributions of both radial orders. This method, which fits 12 parameters at once for a large number of points in the spectrum, is highly time consuming, which makes it difficult to use. For this work we use a 4-parameter fitting method for (U_x^n, U_y^n), keeping the other parameters fixed after an initial 12-parameter fit. (González Hernández et al. 1998b).

4.2. Inversion Process

The velocities obtained from the fitting procedure have a different dependence in frequency for each n. Through the dispersion relation, this is equivalent to having a set of velocities associated with different oscillation modes. It is then necessary to invert these velocities to infer the depth dependence. An inversion method based on a least-squares piecewise constant fit with second-derivative smoothing has been applied to solve the inverse problem. The set of kernels used for the inversions was derived from a standard solar model by Bahcall & Ulrich (1988). The method was developed by F. Hill and D. Gough and has been tested in previous applications of ring diagram analysis (González Hernández 1998c).

5. RESULTS

Applying the ring diagram analysis method to all of the sections described above, we obtained the average horizontal velocities, U_x and U_y, as a function of depth in a range of about $0.97R_\odot$ through the surface for each region. To study the meridional flows, we isolated the latitudinal component U_y. In figure 2 we show the results at different depths for each longitude (right and left) and

sphere was rotating slightly more rapidly than the northern (Giles & Duvall 1998).

The following section outlines the method of applying time-distance helioseismology to large-scale flows. In the Results section, we show new results which extend our previous work to cover longer time periods and greater depths.

2. METHODS

Time-distance helioseismology relies on the measurement of acoustic wave travel times to infer details of the sun's interior structure (Duvall et al. 1997). The travel time between two points on the solar surface is measured by computing the temporal cross correlation of their velocity signals. The location of the peak in the cross correlation is then interpreted as the time required for a sound wave to propagate from one point to the other. In practice, it is necessary to average together cross correlations for many pairs of points. The travel time is determined by fitting a Gabor wavelet to the average cross correlation.

To measure flows, it is necessary to measure wave travel times in opposite directions along the same ray path. The time difference $\delta\tau$ between the two travel times is then related to the flow velocity $\mathbf{v}$ by

$$\delta\tau \simeq -2 \int_\Gamma \frac{\mathbf{v} \cdot \hat{\mathbf{n}}}{c^2} ds \quad (1)$$

where $\hat{n}ds$ is the length along the ray path Γ, and c is the sound speed.

By choosing different pairs of end points, one can select different ray paths, and hence probe the velocity in specific directions and at various locations. For example, to measure the meridional flow, it is necessary to choose pairs of points which lie along the same (or nearly the same) line of longitude (figure 1). In this case, the travel time difference is only sensitive to the north-south component of the flow, and

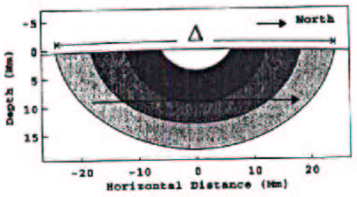

Figure 2. In the interpretation of time-distance measurements, acoustic waves are assumed to travel along narrow ray paths, which are determined by the sound speed profile below the surface. Waves which travel a larger distance Δ penetrate deeper into the interior. The solid curved arrow represents a hypothetical meridional flow through the region of ray propagation.

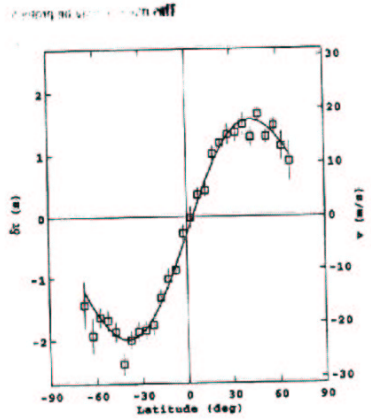

Figure 3. The squares represent the measured time differences $\delta\tau$ between southward and northward travel times, for a range of central latitudes λ. A positive time difference indicates a northward flow; hence the observations clearly show a poleward meridional flow in both hemispheres, with a small southward flow across the equator. The corresponding flow velocity (right-hand axis) was computed using equation (1) by assuming a uniform, horizontal flow throughout the region of propagation. The solid curve is a three-term least squares fit to the data (see text).

is not affected by the rotation.[1] Conversely, the rotation can be measured by choosing endpoints with the same (or nearly the same) latitude.

By varying the separation Δ between the endpoints, it is possible to probe different depths beneath the surface (figure 2). Thus, by measuring the travel times at different distances Δ and latitudes λ, we can determine the velocity $\mathbf{v}(r, \lambda)$ from equation (1).

For the results which follow, we have used Doppler images from the Michelson Doppler Imager (MDI) on SOHO. Almost all of the current work has been done with full-disk images from the summer of 1996 (May 24 – July 23). These images have a resolution of 2 arcseconds at disk center and a cadence of one minute. In spatial extent, the area studied extended to ±80° latitude and spanned 60° in longitude. This area was remapped onto a rectangular grid with pixels equally spaced in longitude and sine of latitude. The remapping was done for the entire two-month time series in eight-hour segments, and the cross correlations were computed (as described in figure 1) for each segment independently. In order to improve the signal-to-noise characteristics, the resulting cross correlations were averaged together in time before determining the travel times.

[1] Note that although the endpoints in figure 1 do not all have the same longitude, the distribution of pixels is chosen to be symmetric with respect to the line of longitude that passes through P. The effect of rotation thus cancels out.

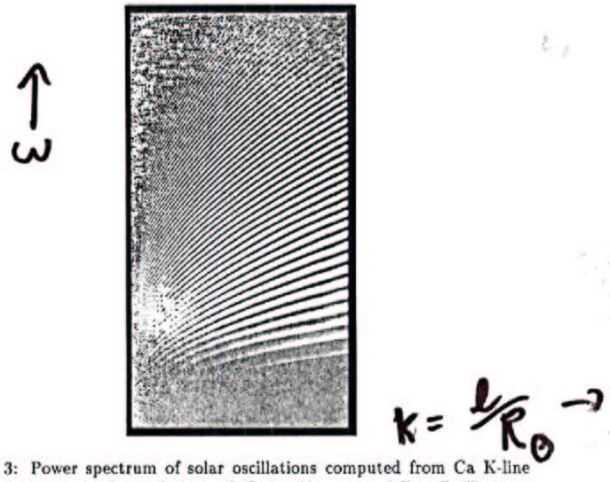

Figure 3: Power spectrum of solar oscillations computed from Ca K-line movies taken at the South Pole, by Jefferies, Harvey, and Duvall. Horizontal wavenumber runs from left to right; temporal frequency increases from bottom to top. In order of increasing frequency the ridges visible in the figure correspond to p-modes of radial order $n = 1, 2, 3, \ldots$. The highest frequency plotted corresponds to a period of 2 min. (Courtesy S. M. Jefferies.)

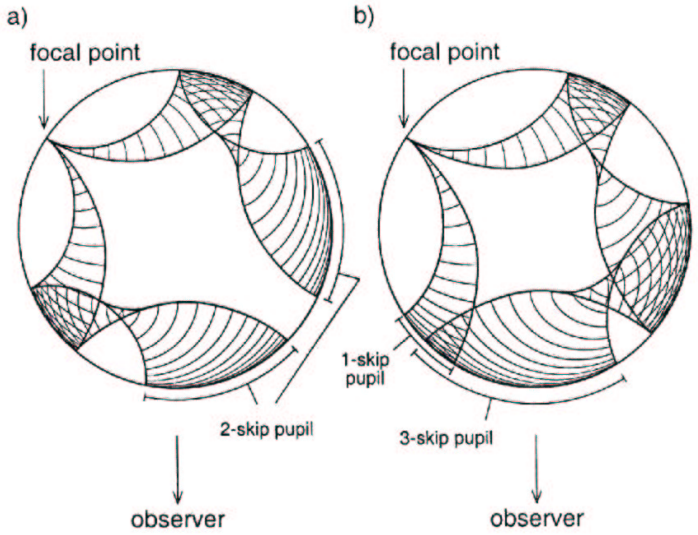

Fig. 1.— Far-side imaging for focal points significantly away from the antipode of disk center (ADC), showing (*a*) the limitations of using a 2–skip correlations, and (*b*) the advantages of using one/three–skip correlations. Both panels show cross sections of the solar interior, as viewed from above the north pole of the Sun. Wavefronts emanate from a far-side point source (focal point), located at 55° from ADC, at intervals of 286 s within a corridor of trajectories reflecting a number of times from the solar surface to arrive at the near-side. To avoid clutter in the diagram, the pupils illustrated in panel *b* are actually narrower than those used in the data analysis.

$$d(\underset{\sim}{x},t) \longleftrightarrow d_{\underset{\sim}{k}\omega} \qquad (\underset{\sim}{x} = x, y \; ; \; \underset{\sim}{k} = k_x, k_y)$$

$$\langle d(\underset{\sim}{x},t)\, d(\underset{\sim}{x}+\delta\underset{\sim}{x},\, t+\delta t)\rangle$$

$$\longleftrightarrow \langle d_{j\sigma}\, d^{*}_{\underset{\sim}{k}\omega}\rangle \equiv \Gamma_{j\sigma,\underset{\sim}{k}\omega}$$

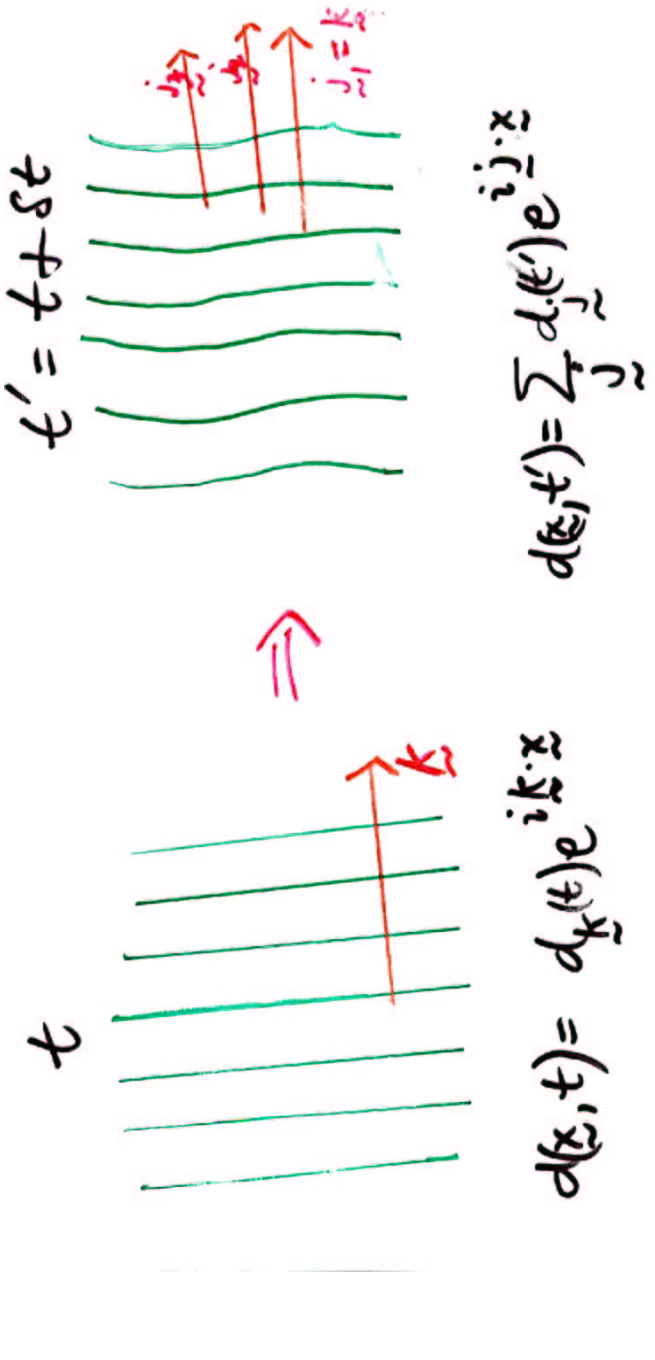

$$d'_{\underset{\sim}{j}} = S_{\underset{\sim}{jk}}\, d_{\underset{\sim}{k}}$$

$$S_{\underset{\sim}{jk}} \propto V_{\underset{\sim}{g}} \quad , \quad \underset{\sim}{g} = \underset{\sim}{j} - \underset{\sim}{k}$$

→ reality:

$$d'_{\underset{\sim}{j}} = \sum_{\underset{\sim}{k}} S_{\underset{\sim}{jk}}\, d_{\underset{\sim}{k}} + g_{\underset{\sim}{j}}$$

$$\langle d'_{\underset{\sim}{j}} d^*_{\underset{\sim}{k}} \rangle = S_{\underset{\sim}{jk}} \langle d_{\underset{\sim}{k}} d^*_{\underset{\sim}{k}} \rangle$$

~~~

$$d(\underset{\sim}{x}, t) \hookleftarrow d_{\underset{\sim}{k}\omega}$$

$$\langle d_{\underset{\sim}{j}\sigma}\, d^*_{\underset{\sim}{k}\omega} \rangle = \Gamma_{\underset{\sim}{j}\sigma, \underset{\sim}{k}\omega}$$

$$y = Y(x) + \varepsilon \quad , \langle \varepsilon \rangle = 0$$

$$\leftrightarrow \langle y \rangle = Y(x)$$

choose x to min. $|\varepsilon|^2$

~~~

$y = d$? -- No!

$(d = \{ d_{\underset{\sim}{k}\omega} \})$

$$y = d\, d^\dagger = \begin{pmatrix} d_{\underset{\sim}{k}\omega_1} \\ d_{\underset{\sim}{k}_2\omega_2} \\ \vdots \\ d_{\underset{\sim}{k}_N\omega_N} \end{pmatrix} \left(d^*_{\underset{\sim}{k}_1\omega} \; d^*_{\underset{\sim}{k}_2\omega_2} \cdots d^*_{\underset{\sim}{k}_N\omega_N} \right)$$

↓

$$y = Ax + x^\dagger B x + \ldots \ldots + \varepsilon$$

$$\approx Ax + \varepsilon \rightarrow \min |y - Ax|^2$$

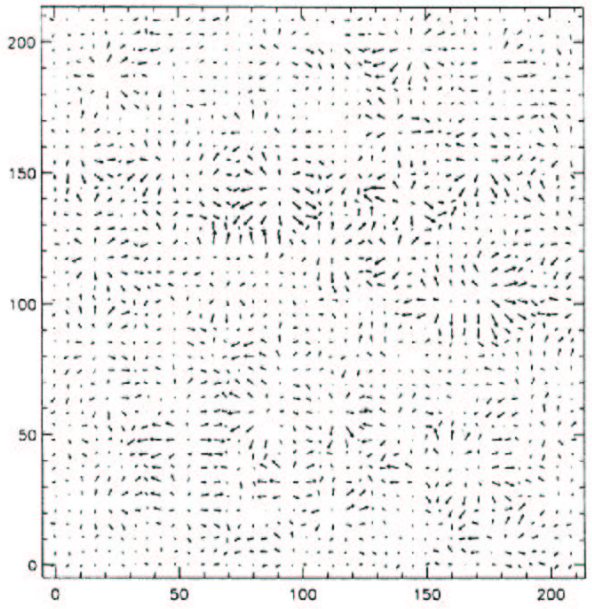

Fig. 2.— Horizontal velocity map of supergranular flow, based on inversion of helioseismic data. The area shown is the same as in Fig. 1 with the distance scale in Mm. The velocity scale is $\approx 0.15\,\mathrm{km\,s^{-1}}$ per Mm of displacement in the plot.

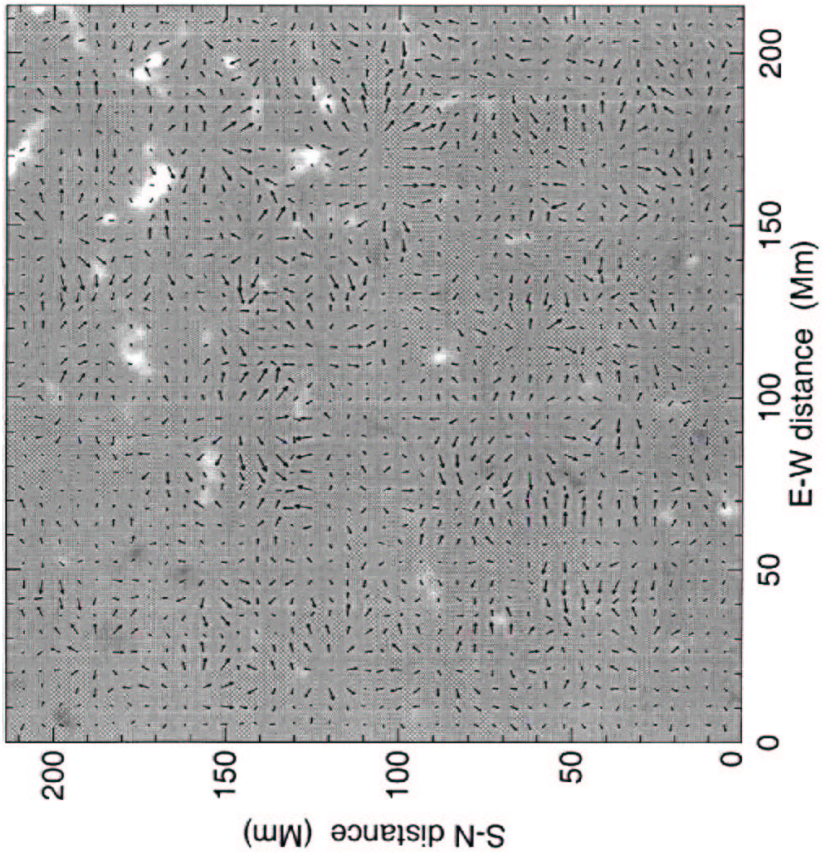

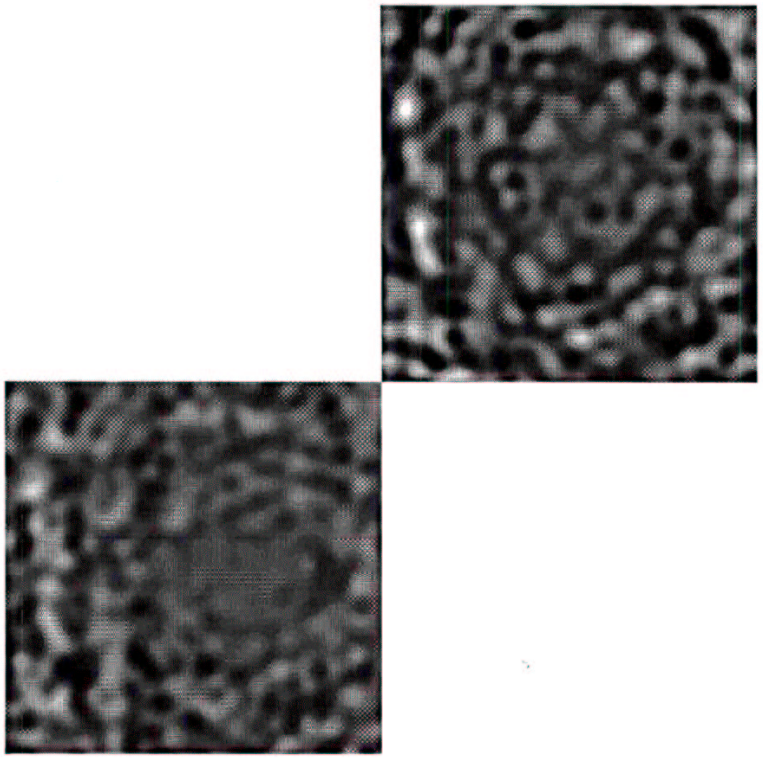

Seismic